

Cyclic Experiments and Global Buckling Design of Steel-Angles-Assembled Buckling-Restrained Braces

Jing-Zhong Tong (✉ tongjz@zju.edu.cn)

Zhejiang University <https://orcid.org/0000-0003-3190-518X>

En-Yuan Zhang

Zhejiang University

Yan-Lin Guo

Tsinghua University

Chao-Qun Yu

Zhejiang University

Research Article

Keywords: Steel-angles-assembled buckling-restrained braces, Hysteretic behavior, Cyclic experiments, Finite element analysis, Restraining ratio, Global buckling design

Posted Date: December 30th, 2021

DOI: <https://doi.org/10.21203/rs.3.rs-1204081/v1>

License:   This work is licensed under a Creative Commons Attribution 4.0 International License.

[Read Full License](#)

Version of Record: A version of this preprint was published at Bulletin of Earthquake Engineering on April 4th, 2022. See the published version at <https://doi.org/10.1007/s10518-022-01389-w>.

Cyclic experiments and global buckling design of steel-angles-assembled buckling-restrained braces

Jing-Zhong Tong ^{a,b,*}, En-Yuan Zhang ^a, Yan-Lin Guo ^b, Chao-Qun Yu ^a

^a Institute of Advanced Engineering Structures and Materials, Zhejiang University, Hangzhou 310058, China

^b Department of Civil Engineering, Tsinghua University, Beijing 100084, China

Abstract: Compared with traditional BRB, the steel-angles-assembled buckling-restrained brace (SAA-BRB) is an innovative BRB with light-weight, accurate control of the geometrical dimensions, easy installation and convenient disassembly. The SAA-BRB is composed of an external restraining system and a cruciform-sectional inner core. The external restraining system is assembled by four steel angles with the connection of high-strength bolts, and the spacers are installed between the inner core and the restraining system. In this study, the hysteretic behavior of SAA-BRB was investigated by experiments and finite element (FE) simulations. Firstly, three SAA-BRB specimens with different restraining ratios were tested under cyclic loads to investigate the hysteretic performance. It was found that all specimens exhibited stable responses and satisfactory energy-dissipating capabilities during the whole loading process. Then, a refined FE model was established, and its validity in predicting the hysteretic responses of SAA-BRB was verified by the experiments. Moreover, based on the yielding criteria of the outmost fiber for the restraining member section, a design formula for the restraining ratio requirements to avoid global buckling of the SAA-BRB was deduced. Finally, extensive parametric analysis was conducted to verify the accuracy of the design formula by changing the geometric dimensions (the restraining ratio) of models. It was found that the proposed formula for the restraining ratio requirement could lead to a conservative prediction with reasonable accuracy, thus providing valuable references for global buckling design of SAA-BRBs in engineering practice.

Keywords: Steel-angles-assembled buckling-restrained braces; Hysteretic behavior; Cyclic experiments; Finite element analysis; Restraining ratio; Global buckling design

* Corresponding author
E-mail address: tongjz@zju.edu.cn

Nomenclature

Symbol	Description
A_1	Cross-sectional area of a single steel angle
A_0	Cross-sectional area of the external restraining system
A_c	Cross-sectional area of the steel core
b	Width of yield segment of the inner core
b_a	Length of the steel angle flange
b_1	Width of strengthened segment of the inner core
f_{yr}	Yield stress of the external restraining system
f_{yc}	Yield stress of the inner steel core
F_y	Yield load of the specimen
F_{max}	Maximum load of the specimen
g	Gap size between the steel core and restraining system
h_{ar}	Distance between the edge of restraining system and the bolts circle center
H	Height of frame connected with the BRB
I_0	Moment of inertia regarding the external restraining system as a whole
I_1	Moment of inertia of a single steel angle
K_i	Axial secant stiffness
l	Length of SAA-BRB
l_0	Length of the restraining system
l_y	Length of yield segment of the inner core
l_u	Length of unrestrained segment of the inner core
l_t	Length of transition segment of the inner core
l_s	Length of strengthened segment of the inner core
Δl_y	Axial deformation of the BRB
Δ_y	Yield displacement of the specimen
Δ_{max}	Maximum displacement of the specimen
$+\Delta_i$	Displacement corresponding to tensile peak point at i-th hysteretic cycle

$-\Delta_i$	Displacement corresponding to compressive peak point at i-th hysteretic cycle
l_1	Bolts spacing along the longitudinal direction
L	Length of frame connected with BRB
M_{\max}	Maximum bending moment at mid-span of the restraining system
P_{cr}	Euler buckling load of BRB
$P_{cr,0}$	Euler buckling load of the external restraining system of ordinary BRB
$P_{cr,c}$	Euler buckling load of the inner core
$P_{cr,r}$	Euler buckling load of the external restraining system of SAA-BRB
P_y	Yield load of the inner core
$P_{c\max}$	Load corresponding to compressive peak point of the hysteretic curve
$P_{t\max}$	Load corresponding to tensile peak point of the hysteretic curve
$+P_i$	Load corresponding to tensile peak point at i-th hysteretic cycle
$-P_i$	Load corresponding to compressive peak point at i-th hysteretic cycle
$S_{(ABC+CDA)}$	Area enclosed by a single hysteretic curve and the abscissa
$S_{(OBE+ODF)}$	Triangle area enclosed by a dotted line and the abscissa
t	Thickness of the inner core
t_a	Thickness of steel angle
v_0	Amplitude of the initial geometrical imperfection of the SAA-BRB
v_{\max}	Lateral maximum deformation at mid-span of the restraining system
W	Plastic section modulus of the external restraining system of SAA-BRB
ω	Reduction factor of global buckling load of external restraining system
ζ	Restraining ratio
$[\zeta]$	Restraining ratio requirements
λ_0	Slenderness ratio regarding the external restraining system as a whole
λ_1	Slenderness ratio of a segment of single chord member
σ_{\max}	Maximum normal stress of the external restraining system
λ_c	Slenderness ratio of the inner core
α	Angle between the BRB and its connected frame beam

$[\varepsilon_c]$	Maximum axial strain requirement of the BRB
φ	Ratio of the inner core yield segment length to BRB length
β	Compression strength adjustment factor
ζ_{eq}	Equivalent viscous damping ratio

28

29 **1 Introduction**

30 As a high-performance member with excellent lateral resistance and energy dissipation
31 capacity, buckling-restrained brace (BRB) has been widely used in engineering practice in
32 many countries such as Japan, the US, and China over the years (Kiggins and Uang 2006;
33 Tremblay et al. 2006; Zhao et al. 2017). Generally, the BRB is composed of an inner steel core
34 encased by an external restraining system. The inner core is used to bear the axial load, and the
35 external member is used to limit the lateral displacement of the inner core to prevent it from
36 global buckling (Tong et al. 2020). In the design of BRB, the inner core should reach its full-
37 sectional yield load without undergoing global buckling/local failure mode, ensuring the
38 excellent load-carrying performance and energy-dissipating capacity of BRBs (Black et al.
39 2004; Eryasar and Topkaya 2010; Kiggins and Uang 2006; Tong and Guo 2018).

40 Under regular use or minor earthquakes, BRB can provide sufficient lateral stiffness and
41 horizontal bearing capacity for the frame structure as common braces, and the inner core is in
42 an elastic working state. Under the action of severe earthquakes, BRB can fully develop its
43 plasticity and energy dissipation capacity, reducing damage to the main frame structure
44 (Ariyaratana and Fahnstock 2011; Takeuchi et al. 2010; Zhao et al. 2013). Therefore, the
45 application of BRB not only avoids the global buckling of ordinary braces under severe
46 earthquakes, but achieves excellent energy-dissipating performance to protect the frame
47 structure (Shi et al. 2018).

48 The concept of BRB was first proposed by Yoshino and Karino (1971). In that study, a
49 member with steel plates embedded in reinforced concrete shear walls was proposed. Its
50 working principle is to restrain the buckling of the embedded steel plate through the external
51 concrete wall panel. However, this is not conducive to the material utilization because only
52 the diagonal strip-shaped area of the concrete wall can directly limit the lateral deformation of
53 the embedded steel plate. In this consideration, BRB has gradually evolved into a type in which
54 a slender external restraining system constrains the inner core to further improve the utilization
55 of material. In early development stage of this type of BRBs, a typical restraining member is
56 composed of concrete-filled steel tube or reinforced concrete (Mochizuki et al. 1979; Nagao et

57 al. 1992). Since the restraining system is used to limit the lateral deformation of the inner core,
58 a thin layer of unbonded material should be installed at the interface between the inner core
59 and its surrounding concrete to avoid axial force transmission (Fujimoto et al. 1990; Ju et al.
60 2009; Palazzo et al. 2009). However, complex construction procedures caused by wet concrete
61 work, heavy self-weight and inconvenient disassembly result in difficulties when repairing the
62 BRB after an earthquake (Ju et al. 2009; Shi et al. 2018). To solve these problems, researchers
63 proposed BRBs with all-steel composition and conducted experimental and numerical studies
64 (Guo et al. 2016; Guo et al. 2017a, b; Hosseinzadeh and Mohebi 2016; Jia et al. 2017; Judd et
65 al. 2016; Mirtaheri et al. 2017). The all-steel BRB is mainly characterized by a steel core with
66 a circular section or H-section and a restraining member of a circular or square steel tube. Due
67 to its all-steel composition, there is no need for unbonded material at the interface between the
68 inner core and the restraining member as an air gap could be precisely controlled during its
69 fabrication (Guo et al. 2017a; Jia et al. 2017; Mirtaheri et al. 2017). Besides, the self-weight of
70 all-steel BRB is significantly reduced compared with the traditional BRB composed of an inner
71 steel core with the encasement of concrete-filled steel tube. Furthermore, to satisfy the
72 requirements of high-rise buildings or long-span structures with popularity in recent years,
73 assembled BRBs with bolt-connected restraining systems were proposed and investigated by
74 numerous researchers (Chou and Chen 2010; Dehghani and Tremblay 2018; Ding 2014; Guo
75 et al. 2018; Jiang et al. 2017; Metelli et al. 2016; Tong and Guo 2018; Chou et al. 2019). Chou
76 and Chen (2010) developed a sandwiched assembled BRB with an inner core encased by two
77 identical restraining members connected with high-strength bolts, and four BRB specimens
78 were tested to investigate the load-carrying performance. Dehghani and Tremblay (2018)
79 proposed an all-steel assembled BRB composed of a flat plate core and a rectangular restraining
80 member with a hollow steel section. The stable seismic performance and high post-yield
81 stiffness of this BRB were examined by experiments. Jiang et al. (2017) developed a pinned
82 double-rectangular tube assembled BRB, which exhibited satisfactory energy-dissipating
83 performance under repeated axial-tension loading. Guo et al. (2018) proposed an assembled
84 BRB in which the restraining member consists of four steel channels assembled by bolts. A FE

85 model that could well predict the hysteretic responses was established and a design procedure
86 was proposed subsequently. For assembled BRBs, the external restraining system generally
87 includes multiple components connected by high-strength bolts. The advantages of assembled
88 BRB include: (1) the fabrication of BRB with the bolt connection is convenient and quick; (2)
89 the BRB can be easily disassembled, reducing the difficulty in transportation and erection; (3)
90 the damaged core can be easily replaced in the post-earthquake structure due to the feature of
91 easy disassembling. It should be noted that the discrete arrangement of the connecting bolts
92 will weaken the rigidity of the restraining member in the design of assembled BRBs.

93 In this paper, a new type of assembled BRB called steel-angles-assembled BRB (SAA-
94 BRB) was studied. The SAA-BRB consists of a cruciform-sectional steel core and a restraining
95 system composed of four steel angles. The cyclic loading experiment was carried out on three
96 specimens to investigate the load-carrying performance and hysteretic response of SAA-BRB.
97 Besides, a finite element (FE) model of SAA-BRB was established, and the comparison against
98 experimental results verified the feasibility of the model. Moreover, the theoretical design
99 formula with restraining ratio requirements to prevent SAA-BRB from global buckling was
100 derived. Finally, extensive FE simulations were performed to validate the proposed design
101 formula.

102 **2 Cyclic experiments**

103 2.1 Experimental specimens

104 Three SAA-BRB specimens were designed to experimentally investigate their hysteretic
105 responses. Fig. 1 shows the construction details of SAA-BRB specimens, which consists of an
106 inner steel core with a uniform cruciform-section and a restraining system as well as spacers.
107 The external restraining system is composed of four steel angles assembled by high-strength
108 bolts (M16). The spacers with holes for the bolts to pass through are installed between the steel
109 angles. The inner core can be divided into yield segment and unrestrained segment composed
110 of a transition segment and a strengthened segment along its longitudinal direction. The
111 unrestrained segment of the core was enhanced at both ends by expanding its cross-sectional
112 size, and it was welded with a flange to prevent it from local buckling. Besides, the stiffened

113 plates were set at the end of each steel angle along the longitudinal direction to enhance the
 114 integrity of the external restraining member. According to Chinese design code GB50017 (GB
 115 2017), the slenderness ratio of the core λ_c should be greater than $5.07b/t$ to prevent the torsional
 116 buckling failure of SAA-BRB. Additionally, the stoppers (i.e. displacement limitation fastener)
 117 were designed and arranged on each side of the mid-span of the core by welding to inhibit the
 118 restraining system from sliding longitudinally along the core.

119 Specimens S-1, S-2 and S-3 were similar in geometrical configuration, and the design
 120 parameters of each specimen are tabulated in Table 1. For all specimens, SAA-BRB length, l ,
 121 and restraining system length, l_0 , were 2400 mm and 2100 mm, respectively. The steel angle
 122 width b_a of Specimen S-1 was 80 mm, and those of Specimens S-2 and S-3 were 90 mm. Steel
 123 angle thickness t_a was 6 mm for each specimen. The cruciform-sectional core member width,
 124 b , was 100 mm for Specimens S-1 and S-2 while 110 mm for Specimen S-3. Inner core
 125 thickness, t , was 22 mm for each specimen.

126 To avoid the axial load sustained by the inner core being transmitted to the restraining
 127 system, hard rubbers with a thickness of 1.2 mm were installed between the steel core and four
 128 steel angles. The spacer thickness of all specimens was 25 mm, and the spacer widths in the
 129 transverse direction of the cross-section and the longitudinal direction were 48 mm and 42 mm,
 130 respectively.

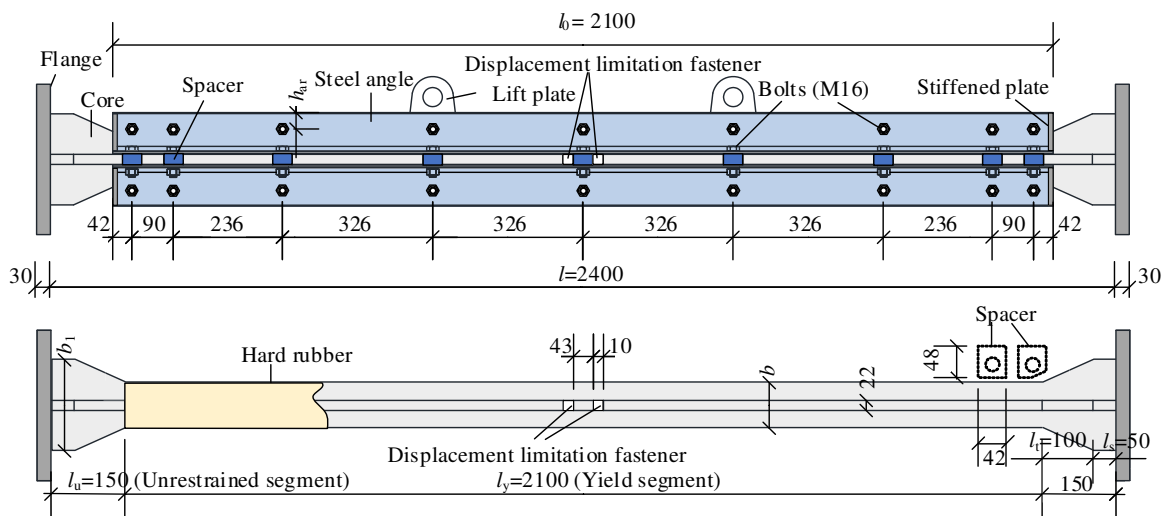


Fig. 1 Construction details of SAA-BRB specimens

131
132

Table 1 Design parameters of SAA-BRB specimens

Specimen no.	b (mm)	b_1 (mm)	$b_a \times t_a$ (mm)	h_{ar} (mm)	g (mm)	l_0	f_{yr} (MPa)	f_{yc} (MPa)	ζ
S-1	100	200	80×6	25	1	2100	380	288	1.86
S-2	100	200	90×6	35	1	2100	380	288	2.47
S-3	110	220	90×6	35	1	2100	380	288	2.22

133 2.2 Experimental setup and loading protocol

134 The MTS hydraulic servo testing machine was used for applying cyclic loads. Fig. 2
135 presents the experimental setup consisting of two reaction frames anchored to the strong floor
136 and test specimens loaded via a 600 t actuator with an in-line load cell. At both ends of each
137 specimen, the flange with Q345 steel plate is connected to the cross-shaped connecting plate
138 using high-strength bolts, and the cruciform-shaped connecting plate is also connected to the
139 actuator and the reaction frame with the connection of bolts.

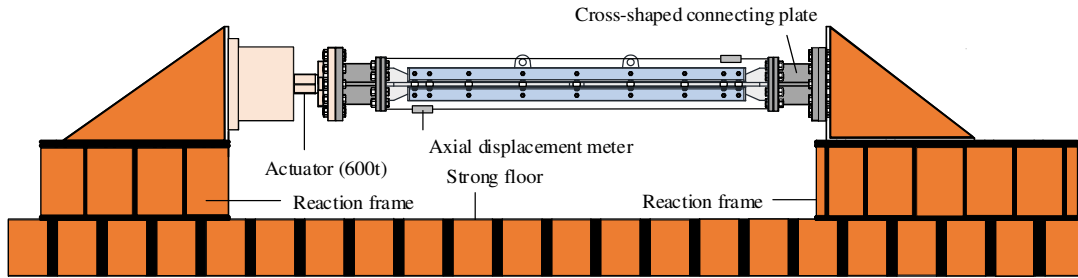


Fig. 2 Experimental setup

140 As shown in Fig. 3, H and L respectively denote the height and length of the frame
141 connected with BRB, α the angle between the BRB and the frame beam, thus the length of the
142 BRB l can be expressed as $l = \sqrt{H^2 + L^2}$. For BRB, the length of the yield segment of the core is
143 l_y , thus the ratio of the core yield segment length to BRB length is denoted as $\varphi = l_y / l$. According
144 to the Chinese code GB50010 (GB 2010) for seismic design of buildings, the maximum drift
145 angle of the frame structure is 1/50. Hence, the maximum axial deformation of the inner core
146 can be expressed as $\Delta l_y = H \cos \alpha / 50$. In engineering practice, axial deformation mainly occurs in
147 the yield segment of the core due to the unrestrained segment of the core being enhanced by
148 increasing its sectional size. Therefore, the maximum axial strain requirement $[\varepsilon_c]$ of the BRB
149 can be expressed as Eq. (1) by assuming that the axial deformation entirely occurs in the yield

150 segment of the core.

$$[\varepsilon_c] = \frac{\Delta l_y}{l_y} = \frac{H \cos \alpha / 50}{\phi H / \sin \alpha} = \frac{\sin \alpha \cos \alpha}{50\phi} \quad (1)$$

151 Assuming that $\alpha=45^\circ$ and $\phi=0.5$, it is calculated as $[\varepsilon_c] = 0.02$. Therefore, the axial strain of
 152 2.0% was determined as the maximum strain in the loading protocol.

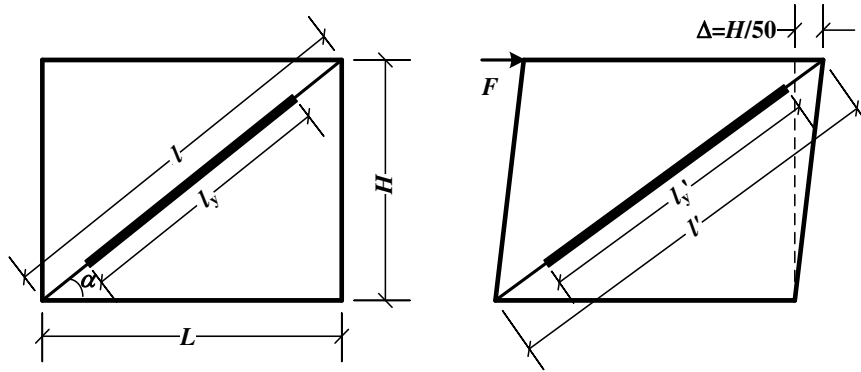


Fig. 3 Calculation of the maximum axial strain requirements

153 Prior to the standard loading process, the axial compressive load of half of the yield load
 154 calculated from the FE model was preloaded to check whether the experimental devices and
 155 measuring instruments were reliable. After that, the standard loading process, in which three
 156 loading cycles with an axial strain of 0.25%, 0.50%, 0.75%, 1.00%, 1.50%, and 2.00%, were
 157 performed successively to the specimens. The axial displacement loading protocol of the
 158 standard loading process for each specimen is tabulated in Table 2. According to this loading
 159 protocol, when the SAA-BRB specimens completed three 2.00% axial strain loadings, the
 160 cumulative plastic ductility would exceed the required ductility of 200 times of the yield strain
 161 as specified in AISC provisions (AISC 2016). The standard cyclic loading protocol of the axial
 162 strain with respect to the cycle number for each specimen is illustrated in Fig. 4.

163 Table 2 Axial displacement loading protocol

Load step	Cycle number	Axial strain	Axial displacement (mm)
1	3	± 0.25%	± 5.0
2	3	± 0.50%	± 10.0
3	3	± 0.75%	± 16.0
4	3	± 1.00%	± 21.0
5	3	± 1.50%	± 32.0
6	3	± 2.00%	± 42.0

164

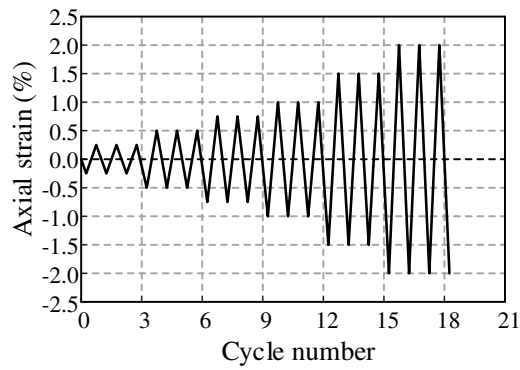


Fig. 4 Cyclic loading protocol

165 2.3 Measurement point arrangements

166 The measuring-point arrangements of strain gauges and displacement meters are
 167 presented in Fig. 5. The strain gauges were installed on the steel angles to record the axial strain.
 168 There were two measured sections: section 1 and section 2, and each section had eight
 169 measuring points. For displacement meters, in addition to two axial displacement meters (as
 170 shown in Fig. 2) used to examine the axial deformation, six lateral displacement meters were
 171 located near the mid-span bolt sets and at the quarter points of the restraining member along
 172 the longitudinal direction.

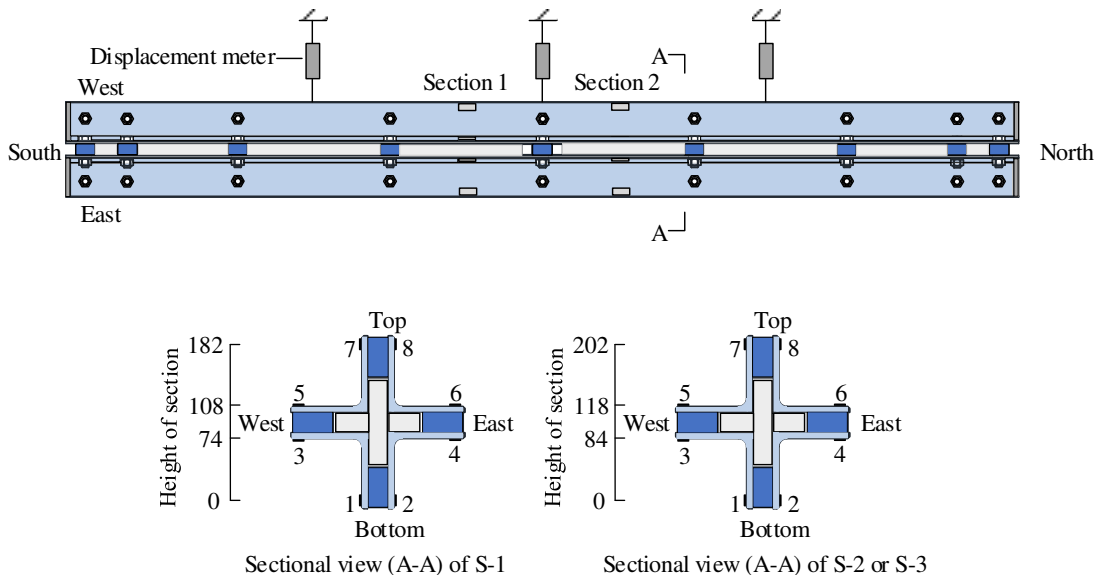


Fig. 5 Measuring-point arrangements

173 2.4 Experimental results

174 2.4.1 Hysteretic curves and skeleton curves

175 It can be seen from Fig. 6 that the hysteretic curves of the three SAA-BRB specimens

176 maintained stable during the whole cyclic loading process, indicating that SAA-BRB has great
177 energy-dissipating capacity under severe seismic effects. Fig. 7 illustrates the deformation
178 condition corresponding to a core strain of 2.0%. It is found that none of the specimens showed
179 global buckling or local buckling. This is because the restraining ratio of each specimen is
180 greater than the corresponding restraining ratio requirement.

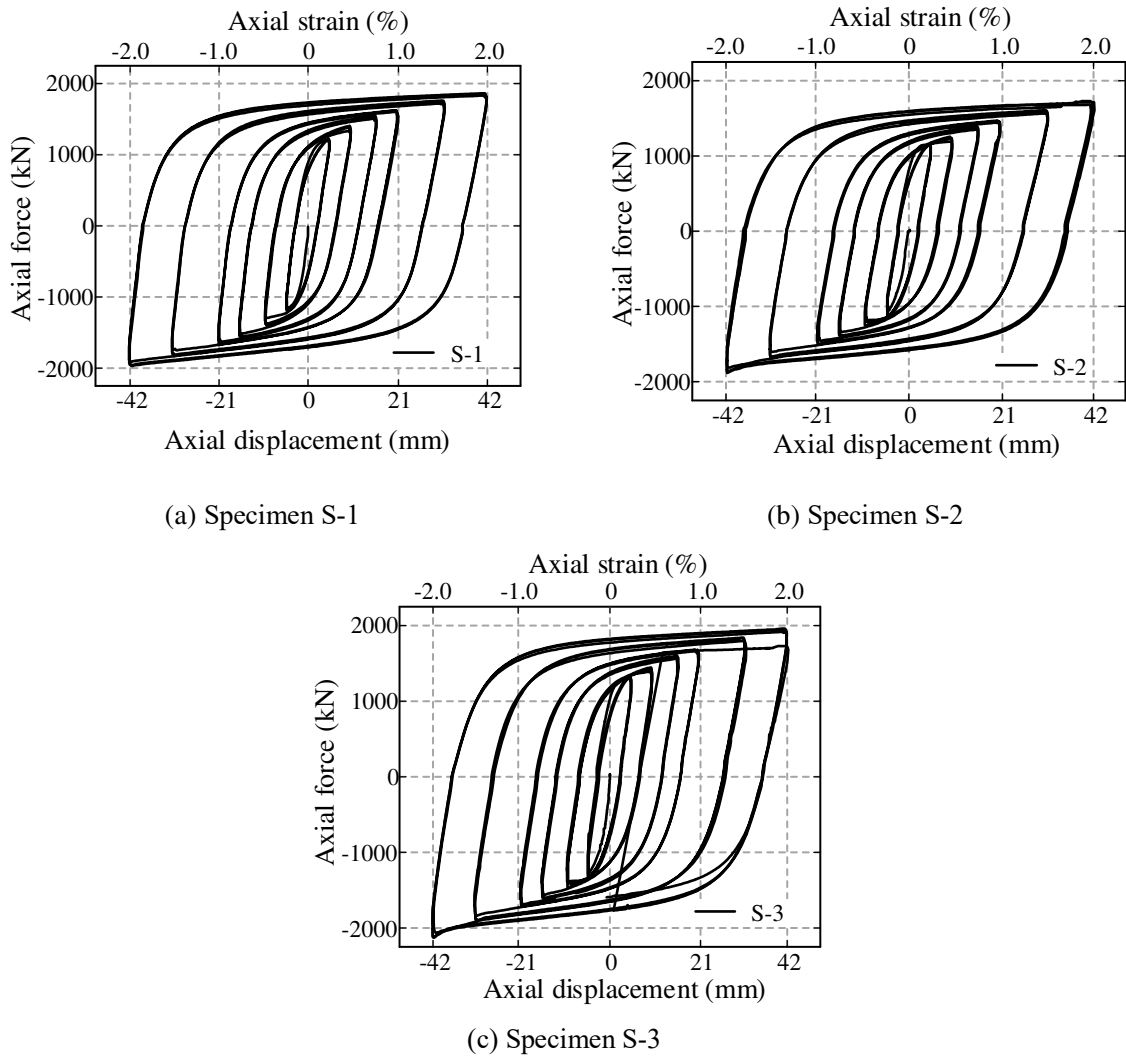
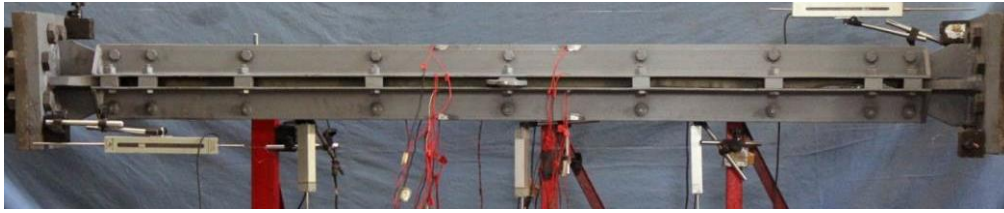


Fig. 6 Hysteretic curves of specimens

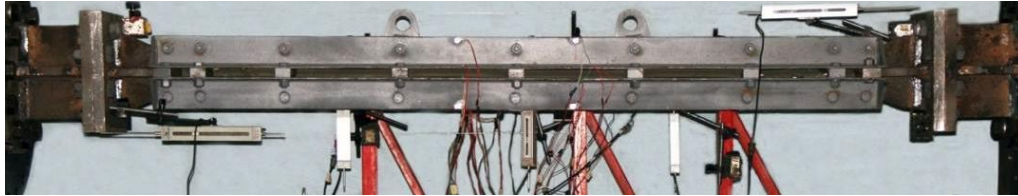
181

182

183



(a) Specimen S-1



(b) Specimen S-2



(c) Specimen S-3

Fig. 7 Deformation condition corresponding to 2.0% axial compression strain

184 The skeleton curves of specimens are depicted in Fig. 8. The displacement and load values
 185 corresponding to the yield and peak points of all specimens are shown in Table 3. When the
 186 specimens reach 2.0% axial strain, the skeleton curves still maintain increasing trends,
 187 indicating that the SAA-BRB specimens have a cyclic effect and great ductility under axial
 188 cyclic loading. Hence, it is conservative to take the peak point of the specimen as the last point
 189 of the skeleton curve to leave enough safety redundancy. In addition, each specimen curve has
 190 obvious inflection points, which are determined as the yield points of the specimen.

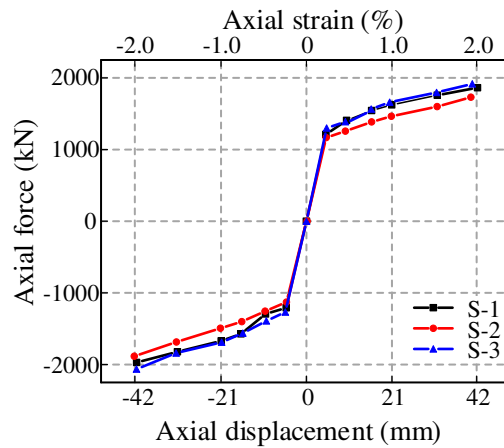


Fig. 8 Skeleton curves of specimens

191

Table 3 Characteristic points and compression strength factors of specimens

Specimen no.	Loading direction	Yield points		Peak points		β
		F_y/kN	Δ_y/mm	F_{\max}/kN	Δ_{\max}/mm	
S-1	Tension	1212.58	4.77	1862.36	41.66	1.06
	Compression	-1208.38	-4.93	-1971.56	-41.33	
S-2	Tension	1166.98	4.80	1730.37	40.04	1.09
	Compression	-1129.18	-4.85	-1884.56	-41.91	
S-3	Tension	1299.57	4.92	1916.36	40.38	1.08
	Compression	-1267.77	-5.13	-2063.96	-41.36	

192 2.4.2 Equivalent viscous damping ratio

193 Fig. 10 illustrates the equivalent viscous damping ratios of all specimens with respect to
194 the hysteretic loop. The energy-dissipating capacity of the specimen can be quantitatively
195 evaluated by the equivalent viscous damping ratio (ζ_{eq}), which can be calculated by Eq. (2). It
196 is seen that the equivalent viscous damping ratio of all specimens generally presents an
197 increasing trend with the increase of the hysteretic loops. Specifically, before the specimens
198 yielded (i.e., before the specimens reached 0.25% axial strain), the values of ζ_{eq} ranged from
199 0.2 to 0.3. As the inner core gradually consumed energy during the loading process, the values
200 of ζ_{eq} increased until they stabilized above 0.4. Moreover, the maximum equivalent viscous
201 damping ratios of the three specimens all exceeded 0.5, demonstrating that all the SAA-BRB
202 specimens exhibited excellent energy-dissipating capacity.

$$\zeta_{\text{eq}} = \frac{1}{2\pi} \cdot \frac{S_{(ABC+CDA)}}{S_{(OBE+ODF)}} \quad (2)$$

203 in which $S_{(ABC+CDA)}$ denotes the enveloping area of the hysteretic loop curve in Fig. 9; and

204 $S_{(OBE+ODF)}$ denotes the area of the triangles OBE and ODF in Fig. 9.

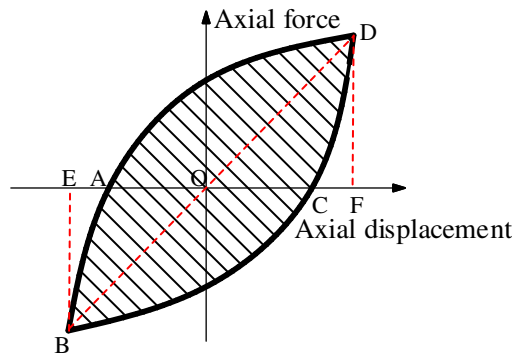


Fig. 9 Calculation of the equivalent viscous damping ratio

205

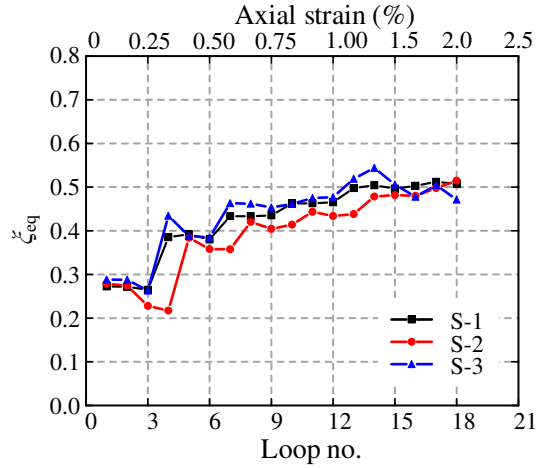


Fig. 10 Equivalent viscous damping ratio of specimens

206 2.4.3 Compression strength adjustment factor

207 The asymmetric response under tension and compression of the SAA-BRB can be
 208 evaluated by the compression strength adjustment factor β , which is defined by Eq. (3) (Jiang
 209 et al. 2017). The larger the β , the more obvious the asymmetric response is. It is calculated that
 210 the β values of the three SAA-BRB specimens are 1.06, 1.09, and 1.08, respectively as
 211 tabulated in Table 3. ANSI/AISC 341-16 (AISC 2016) specified that the factor β shall exceed
 212 unity but be no greater than 1.50. Therefore, it is shown that SAA-BRB has a reasonable
 213 hysteretic response under both tension and compression.

$$\beta = \frac{P_{cmax}^i}{P_{tmax}^i} \quad (3)$$

214 in which P_{cmax}^i and P_{tmax}^i are the loads corresponding to the compressive and tensile peak points
 215 of the hysteretic curve, respectively.

216 2.4.4 Stiffness degradation

217 The stiffness degradation properties of all specimens are shown in Fig. 11. The axial
 218 stiffness degradation curve can reflect the damage history of BRB under cyclic loads.
 219 According to the Chinese code JGJ/T 101-2015 (JGJ 2015), the secant stiffness K_i is used to
 220 express the stiffness of the specimen and its calculation is shown in Eq. (4). The horizontal
 221 coordinate of Fig.11 is the displacement corresponding to the peak point of each loop in the
 222 compressive or tensile directions. It is found that the secant stiffnesses of all specimens are
 223 basically identical at the same load step. In addition, although the axial stiffness of three SAA-
 224 BRB specimens decreased during the loading process, the rate of stiffness degradation

225 gradually slowed down. This shows that the SAA-BRB would not lose its stiffness
 226 instantaneously during loading.

$$K_i = \frac{|\pm P_i|}{|\pm \Delta_i|} \quad (4)$$

227 in which $+P_i$ and $-P_i$ are the loads corresponding to tensile and compressive peak points of the
 228 hysteretic curve at the i -th cycle, respectively; $+\Delta_i$ and $-\Delta_i$ are the displacements corresponding
 229 to tensile and compressive peak points of the hysteretic curve at the i -th cycle, respectively.

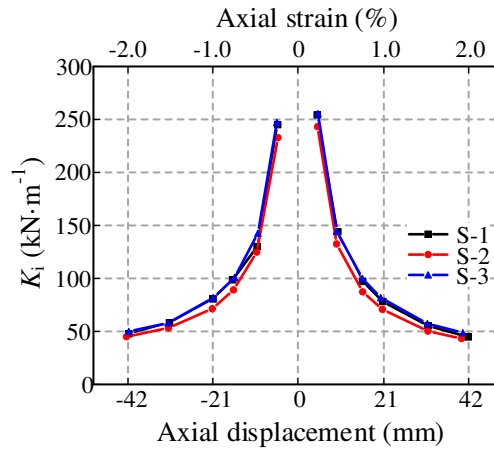
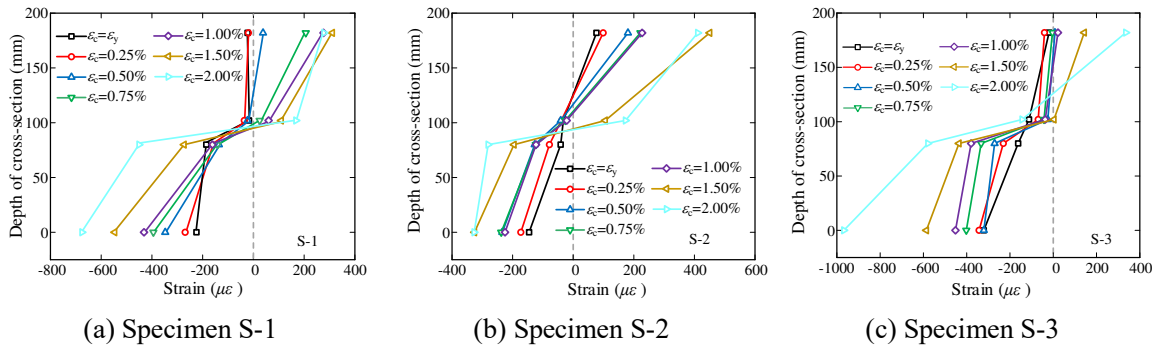


Fig. 11 Curves of axial secant stiffness degradation

230 2.4.5 Longitudinal strain of restraining system

231 Fig. 12 shows the longitudinal strain distribution and development of the external
 232 restraining system of the three specimens. Since the external restraining system was not loaded
 233 when the inner core was under tension, the following analysis focuses on the longitudinal strain
 234 of the external restraining member for the peak compressive displacement in each loading loop.
 235 It is found that the difference between strain data of 1-1 section and 2-2 section is relatively
 236 small, hence the data of 2-2 section is selected for strain analysis. Taking the average value of
 237 a pair of strain data at the same height as the vertical coordinate and the height of the cross-
 238 section as the horizontal coordinate, the distribution of the longitudinal strains on the cross-
 239 section is plotted. It can be seen from Fig. 12 that the major bending direction of SAA-BRB
 240 specimens is the up and down direction. Moreover, it is found that all strain values were less
 241 than the yield strain (i.e., $1670 \mu\epsilon$ for Q345 steel), indicating a good consistency with the stable
 242 load-carrying capacities of these specimens during the loading process as shown in Fig. 7.
 243 Theoretically, the strain distribution of the cross-section of the external restraining member is

244 strictly linear if the restraining system can be regarded as a fully flexural member. However,
 245 the sectional strain distribution of each SAA-BRB specimen depicted in Fig.12 shows that the
 246 linearity is violated. This indicates that significant shear deformation exists in the restraining
 247 system and the plane-section assumption is inappropriate for the SAA-BRB. This is mainly
 248 caused by the discrete layout of the connecting bolts in the restraining system. When the inner
 249 core was under compression and developed multi-wave buckling mode, lateral thrust effect
 250 existed between the core and restraining system, thus causing friction along their interface.
 251 Hence, part of the axial load of the inner core was transmitted to the restraining system. This
 252 explains that the measured compressive strain is larger than tensile strain in the two measuring-
 253 points which are symmetrical to the midline of the cross-section of each specimen.



255 Fig. 12 Distribution and development of longitudinal strains in restraining system

256 3 FE model and validation

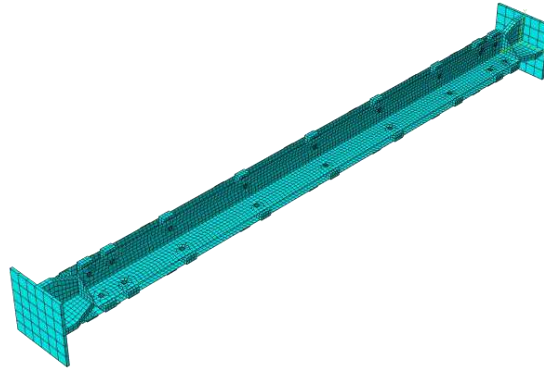
257 3.1 Establishment of hysteretic model

258 In this section, the hysteretic behavior of the SAA-BRBs is simulated with ABAQUS by
 259 establishing a refined FE model. The refined FE model is depicted in Fig. 13. The four-node
 260 shell element (S4R) was used to simulate the steel angles, and the eight-node solid element
 261 (C3D8R) was used to simulate the inner core, spacer and high-strength bolts. It is pointed out
 262 that the high-strength bolts were set as infinitely rigid in the FE model because of their
 263 sufficient stiffness during the cyclic loading process of the experiments. Additionally, an air
 264 gap with a thickness of 1.0 mm on the surface of the inner core was set to ensure that the axial
 265 load transmission between the core and external restraining member was prevented. The
 266 specific geometric parameters of the FE model are identical to those of the specimens.

267 In elastoplastic FE analyses, both geometric nonlinearity and material nonlinearity are

268 considered. It is known that the material nonlinear constitutive relationship mainly consists of
269 yielding and strengthening criteria. In modelling the hysteretic behavior of SAA-BRBs, the
270 von Mises yielding criterion was considered in the material, and a combined isotropic and
271 kinematic hardening model was selected as the strengthening criterion to consider the cyclic
272 effect shown in the experimental results. The yield stress values of the inner core and steel
273 angles were 288 MPa and 380 MPa, respectively. It should be noted that these values were the
274 same as the corresponding data tabulated in Table 1. Based on the suggestion of Guo et al.
275 (2017c), the parameters described below were well validated by the previous experiments for
276 SAA-BRB. For isotropic hardening, a rate factor of 4.2 and a maximum change in yield stress
277 of $Q_{\infty} = 150$ MPa were used in the model. Besides, the relevant moduli and rate factors for
278 kinematic hardening were set as $C_1 = 32$ GPa, $\gamma_1 = 300$; $C_2 = 6$ GPa, $\gamma_2 = 150$; $C_3 = 0.6$ GPa,
279 and $\gamma_3 = 22$.

280 For the contact behavior, the interface between the core and restraining system was
281 simulated by hard contact along the normal direction and friction option along the tangent
282 direction. The hard contact option allowed the interface to separate under tension but not
283 penetrate under compression. The friction coefficient of 0.1 was adopted based on the
284 suggestion of Chou and Chen (2010). In terms of the boundary conditions, both ends of SAA-
285 BRB were modelled as fixed ends since the core was connected with the flange by high-
286 strength bolts. Correspondingly, the rotational degree of freedom of the core at both ends was
287 constrained. Additionally, an initial geometrical imperfection with a magnitude of 1/1000 of
288 the specimen length for the inner core was assigned to the FE model. The loading protocol was
289 the same as that used in the experiment as listed in Table 2, except for the cycle number of each
290 loading level, which was determined to be only one instead of three.



291

Fig. 13 FE model for hysteretic analysis

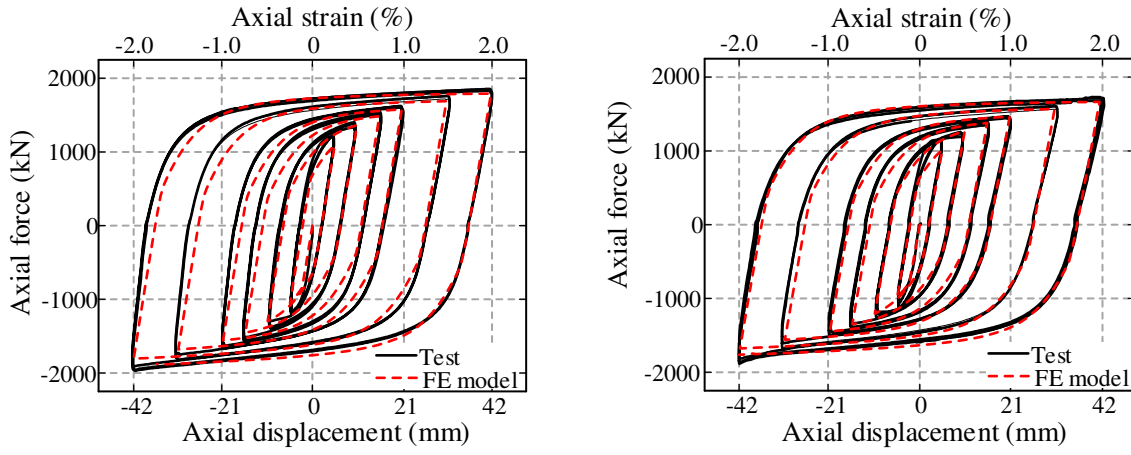
292

293 3.2 Validation of FE model

294 The comparison between the hysteretic curves obtained from FE simulations and
295 experiments are illustrated in Fig. 14. It is seen that the hysteretic curves of the FE models and
296 experiments can fit very well. Moreover, the model in the FE simulation showed the same
297 stable load-carrying performance at the axial strain of 2.0% as the specimen in the experiment.

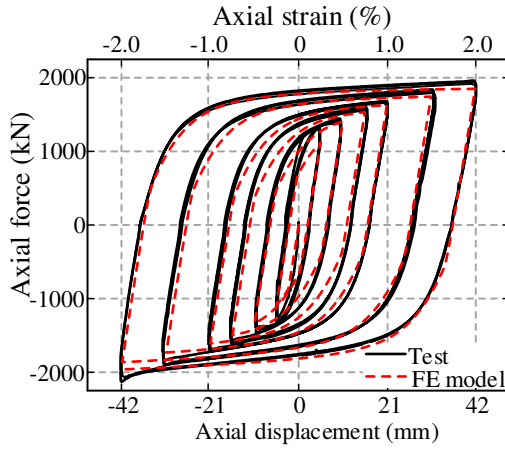
298 Taking the model T-2 as an example, neither the restraining member nor the inner core was
299 observed to undergo global buckling failure, while full cross-sectional yielding of inner core
300 was exhibited at the axial strain of 2.0%, as depicted in Fig. 15. Therefore, the refined FE model
301 developed by software ABAQUS could precisely predict the hysteretic response of the SAA-
302 BRB specimens under cyclic loads.

303 In addition, the unrestrained segment of the core remained elastic, while yielding had
304 spread in the yield segment of the core. This further verifies the feasible design of unrestrained
305 segment of the core by enlarging their cross-sectional size. Moreover, the maximum stress of
306 the steel angles was far less than its yield stress of 380 MPa, indicating that the restraining
307 system had sufficient flexural stiffness to limit the lateral deformation of the inner core.



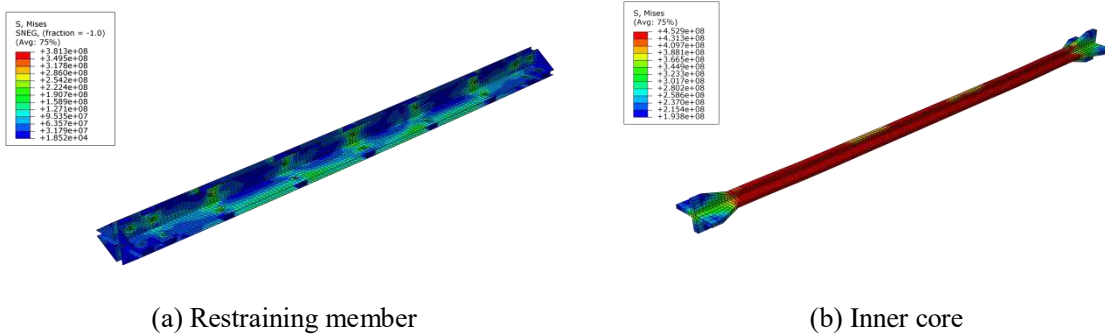
(a) Specimen S-1

(b) Specimen S-2



(c) Specimen S-3

Fig. 14 Comparison of experimental and numerical results of hysteretic curves



(a) Restraining member

(b) Inner core

Fig. 15 Stress distribution of model T-2 at the axial strain of 2.0%

308 4 Theoretical analysis for global buckling design

309 In this section, the formula for restraining ratio requirements of the SAA-BRB is derived.
 310 In designing BRB, a restraining ratio ζ proposed by Fujimoto et al. (1988), reflecting the
 311 restraining effect of the external restraining system on the inner core, is usually used to predict
 312 the global buckling behavior and to examine the load-carrying performance of BRBs. It is

313 known that the restraining ratio ζ is defined as the ratio of the Euler buckling load P_{cr} of BRB
 314 to the yield load P_y of its inner core. The Euler buckling load P_{cr} of BRB can be considered as
 315 the sum of the Euler buckling load $P_{cr,c}$ of inner core and the Euler buckling load $P_{cr,r}$ of
 316 restraining system (Guo et al. 2016). Since the restraining system remains elastic while the
 317 inner core yields during the loading process, leading to the negligible contribution of inner core
 318 in calculating the Euler buckling load P_{cr} of BRB. Therefore, the restraining ratio ζ is
 319 commonly simplified as the ratio of the Euler buckling load $P_{cr,r}$ of the restraining system to
 320 the yield load P_y of the inner core, as expressed by Eq. (5). Theoretically, as long as the
 321 restraining ratio is slightly larger than unity, the cross-sectional strength of inner core can be
 322 fully utilized, thus the BRB can maintain stable without global buckling during the whole
 323 loading process. However, considering the influence of physical defects such as initial
 324 geometric imperfection, residual stress, as well as the gap between the inner core and the
 325 restraining system, the restraining ratio is required to be much larger than unity, indicating the
 326 calculation of the requirements of the restraining ratio would be relatively complicated.
 327 Through a reasonable design, the SAA-BRB will exhibit stable behavior instead of undergoing
 328 global buckling before its inner steel core reaches the full cross-sectional yielding load (Tong
 329 and Guo 2017). Although Tong and Guo (2018) have given the design suggestion about the
 330 restraining requirement of SAA-BRB, there is still a lack of a precise design formula to
 331 determine the restraining ratio as required. During the cyclic loading process, the external
 332 restraining system can be regarded as a flexural member. Therefore, the formula of the critical
 333 restraining ratio, i.e., the calculation of restraining ratio requirement of SAA-BRB, can be
 334 derived by using the yielding criteria of outmost fiber for the restraining system section as the
 335 elastic limit criterion.

$$\zeta = \frac{P_{cr,r}}{P_y} \quad (5)$$

336 in which $P_{cr,r}$ is the Euler buckling load regarding the restraining system as an axial loading
 337 member (Guo et al. 2015); P_y is the yield load of the inner core.

338 For an ordinary BRB with an inner steel core encased by a uniform-sectional restraining
 339 member, the Euler buckling load of the restraining system can be calculated as

$$P_{cr,0} = \frac{\pi^2 EA_0}{\lambda_0^2} \quad (6)$$

340 in which E is the Young's modulus of the restraining member; A_0 is the cross-sectional area of
 341 the restraining member and λ_0 is the slenderness ratio of the restraining member of ordinary
 342 BRB, which can be calculated by Eq. (9).

343 It is known that the arrangement of discretely distributed bolts in the longitudinal direction
 344 would result in a significant shear deformation of the restraining system, thus reducing the
 345 Euler buckling load. Hence, a reduction factor ω is introduced to consider the effect of shear
 346 deformation, as expressed in Eq. (7). The value of ω is closely related to the geometric
 347 dimensions of the assembled BRB and is generally smaller than unity. For the SAA-BRB, Tong
 348 and Guo (2018) introduced the derivation of the formula for ω through numerous FE
 349 simulations and theoretical analysis, which is expressed by Eq. (8). It should be noted that the
 350 derivation of reduction factor ω is based on the equivalence of the restraining system into a
 351 four-chord battened column. In the equivalent relation, the four angle steels were equivalent to
 352 four chord members, and the spacers were equivalent to batten plates (Tong and Guo 2018).

$$P_{cr,r} = \omega P_{cr,0} \quad (7)$$

$$\omega = \left[1 + \frac{\pi^2 \lambda_1^2}{12 \lambda_0^2} + 17.4 \frac{\lambda_1^{0.55}}{\lambda_0^{1.27}} \right]^{-1} \quad (8)$$

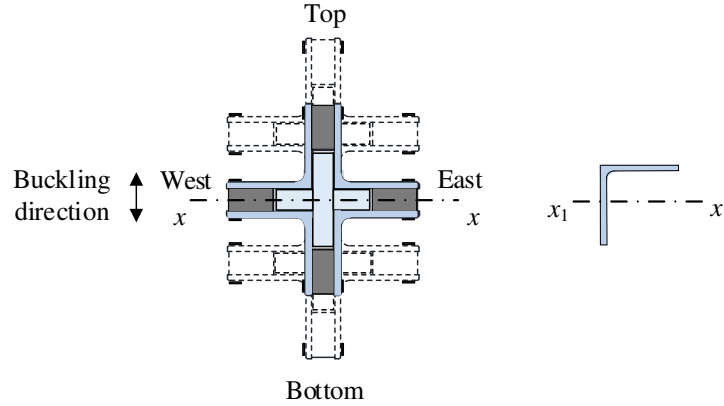
353 in which λ_1 is the slenderness ratio of a single chord member between adjacent batten plates.

$$\lambda_0 = \frac{l_0}{\sqrt{I_0/A_0}} \quad (9)$$

354 in which λ_0 is the slenderness ratio regarding the external restraining system as a member with
 355 a uniform cross-section; l_0 is the length of the external restraining system; I_0 is the moment of
 356 inertia regarding the external restraining system as a whole about the x - x axis and A_0 is the
 357 cross-sectional area of the external restraining system.

$$\lambda_1 = \frac{l_1}{\sqrt{I_1/A_1}} \quad (10)$$

358 in which l_1 is the longitudinal spacing between adjacent high-strength bolts, which is equal to
 359 the spacing between adjacent batten plates; I_1 is the moment of inertia of a single angle about
 360 the x_1 - x_1 axis, A_1 is the cross-sectional area of a single steel angle. Besides, the x - x axis for
 361 calculating the I_0 and x_1 - x_1 axis for calculating the I_1 are shown in Fig. 16.



362

363 Fig. 16 Axis of x - x and x_1 - x_1 for calculation

364 When the load reaches the value corresponding to the yield load of the inner steel core,
 365 the maximum lateral deformation v_{\max} at the mid-span of the restraining system in the
 366 longitudinal direction can be expressed as (Timoshenko et al. 1962)

$$v_{\max} = \frac{v_0 + g}{1 - \frac{P_y}{P_{cr,r}}} \quad (11)$$

367 in which v_0 ($=L/1000$) is the amplitude of initial imperfection and g is the gap between the inner
 368 steel core and the restraining member.

369 When global buckling occurs, the maximum bending moment M_{\max} at the mid-span of the
 370 restraining system can be expressed as

$$M_{\max} = P_y v_{\max} \quad (12)$$

371 Correspondingly, the maximum stress of the restraining system can be calculated by Eq.
 372 (13). It should be aware that the plastic section modulus W is multiplied by the reduction factor
 373 ω to express the weakening effect of discrete bolt connection.

$$\sigma_{\max} = \frac{M_{\max}}{\omega W} \quad (13)$$

374 Based on the yielding criteria of outmost fiber for the restraining system section, the
 375 overall stability requirement of the SAA-BRB subjected to axial compressive load can be
 376 expressed as

$$\sigma_{\max} \leq f_{yr} \quad (14)$$

377 in which f_{yr} is the yield stress of the restraining system.

378 By combining Eqs. (5), (7), and (11) – (14), a calculation for a lower limit of restraining
 379 ratio $[\zeta]$ for SAA-BRB can be expressed as Eq. (15), which is used for global buckling design
 380 of SAA-BRB. For convenience of the design by engineers, $\zeta / [\zeta]$ can be determined as a design
 381 coefficient. When the coefficient $\zeta / [\zeta]$ value exceeds unity, i.e. $\zeta > [\zeta]$, the satisfactory design
 382 of the SAA-BRB can be achieved by preventing its global buckling.

$$\zeta \geq \frac{\omega W f_{yr}}{\omega W f_{yr} - P_y (v_0 + g)} = [\zeta] \quad (15)$$

383 **5 Parametric study and design formula verification**

384 Based on the proposed FE model, 24 FE hysteretic models listed in Table 4 were analyzed
 385 to conduct a parametric study and to verify the accuracy of the proposed formula (Eq. (15)) for
 386 global buckling design of SAA-BRB. The geometric dimensions are listed in Table 4, and the
 387 geometric parameters and material properties of the models are identical with the specimens in
 388 the experimental program. These 24 models were divided into 3 groups, and the core sectional
 389 area of models in each group were identical, and their corresponding values were 4356 mm²,
 390 4796 mm², and 6566 mm², respectively. Besides, the loading protocol in the FE extensive
 391 analysis was determined according to the standard loading stage shown in Fig. 4, yet each
 392 loading step was applied for only one cycle.

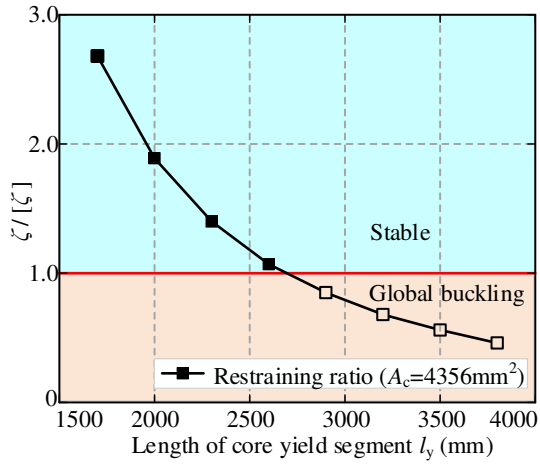
393 Fig. 17 shows the relationship between FE results and the coefficient $\zeta / [\zeta]$. Fig. 18
 394 presents the hysteretic curves of representative FE models. The solid rectangles in Fig.17
 395 represent that the models maintained stable while the hollow rectangles corresponded to
 396 models subjected to global buckling failure. When the $\zeta / [\zeta]$ value is greater than unity, the

397 global buckling failure of the FE model would be prevented and the corresponding hysteretic
398 curves of the models maintained stable; when the $\zeta / [\zeta]$ value is less than unity, the global
399 buckling mode would occur in the FE model. Overall, a critical value (i.e., the value of red line)
400 exists in Fig. 17, below which a stable bearing-capacity would transition to a global buckling
401 mode. Taking model M-3 as an example, its $\zeta / [\zeta]$ value is 1.40. It is seen from Fig. 18(a) that
402 its hysteretic curve is full and symmetrical, indicating a stable bearing-capacity and satisfactory
403 energy-dissipation capability during the whole loading process. Moreover, it is observed from
404 Fig. 19 that the yielding had spread in the core while the restraining system remained elastic.
405 This indicates that the full-sectional yielding load of the inner core could be achieved before
406 reaching 2.0% axial strain. Furthermore, taking model M-13 as an example, its $\zeta / [\zeta]$ value is
407 0.81. It can be seen from Fig. 20 that the model M-13 exhibited global buckling with a single-
408 wave lateral deformation at the load step of 1.5% axial strain, thus severely pinched hysteretic
409 curve was obtained as illustrated in Fig. 18(e). Besides, stress concentrations were observed at
410 the mid-span and both ends of the yield segment of the core, indicating that full cross-sectional
411 yield load of the inner core could not be reached. Therefore, the accuracy of the formula (Eq.
412 (15)) of restraining ratio requirements for global buckling design of SAA-BRBs is validated,
413 which can provide a valuable reference for practical designs.

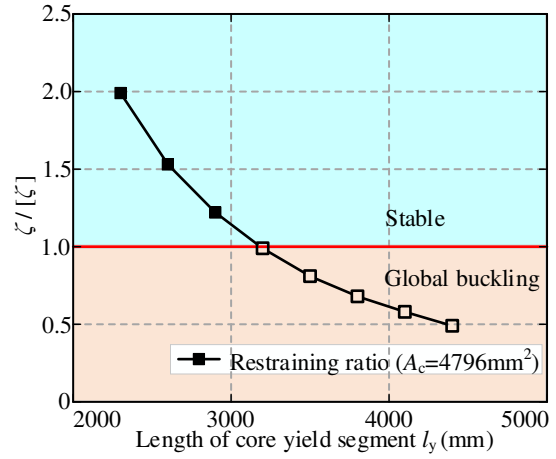
Table 4 Information of hysteretic models and FE results

Group no.	Hysteretic model no.	Geometrical dimensions				A_c (mm ²)	ω	ζ	[ζ]	$\zeta / [\zeta]$	FE results ^a
		l (mm)	l_y (mm)	$b \times t$ (mm)	$b_a \times t_a$ (mm)						
1	M-1	1700	1400	110 × 22	100 × 6	4356	0.548	5.32	1.99	2.68	S
	M-2	2000	1700	110 × 22	100 × 6		0.580	3.82	2.02	1.89	S
	M-3	2300	2000	110 × 22	100 × 6		0.606	2.88	2.06	1.40	S
	M-4	2600	2300	110 × 22	100 × 6		0.627	2.26	2.10	1.07	S
	M-5	2900	2600	110 × 22	100 × 6		0.645	1.82	2.15	0.85	GB
	M-6	3200	2900	110 × 22	100 × 6		0.661	1.50	2.20	0.68	GB
	M-7	3500	3200	110 × 22	100 × 6		0.675	1.25	2.25	0.56	GB
	M-8	3800	3500	110 × 22	100 × 6		0.687	1.07	2.30	0.46	GB
2	M-9	2300	2000	120 × 22	110 × 7	4796	0.595	3.86	1.94	1.99	S
	M-10	2600	2300	120 × 22	110 × 7		0.617	3.03	1.97	1.53	S
	M-11	2900	2600	120 × 22	110 × 7		0.636	2.44	2.01	1.22	S
	M-12	3200	2900	120 × 22	110 × 7		0.652	2.01	2.04	0.99	GB
	M-13	3500	3200	120 × 22	110 × 7		0.666	1.69	2.07	0.81	GB
	M-14	3800	3500	120 × 22	110 × 7		0.679	1.44	2.11	0.68	GB
	M-15	4100	3800	120 × 22	110 × 7		0.690	1.24	2.15	0.58	GB
	M-16	4400	4100	120 × 22	110 × 7		0.700	1.08	2.18	0.49	GB
3	M-17	2300	2000	120 × 22	120 × 8	6556	0.585	4.01	1.96	2.04	S
	M-18	2600	2300	160 × 22	120 × 8		0.607	3.15	2.00	1.58	S
	M-19	2900	2600	160 × 22	120 × 8		0.626	2.54	2.03	1.25	S
	M-20	3200	2900	160 × 22	120 × 8		0.643	2.10	2.06	1.02	S
	M-21	3500	3200	160 × 22	120 × 8		0.657	1.76	2.10	0.84	GB
	M-22	3800	3500	160 × 22	120 × 8		0.670	1.50	2.14	0.70	GB
	M-23	4100	3800	160 × 22	120 × 8		0.682	1.29	2.18	0.59	GB
	M-24	4400	4100	160 × 22	120 × 8		0.692	1.13	2.22	0.51	GB

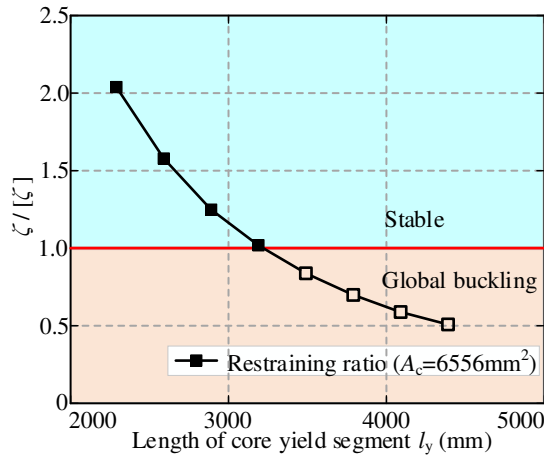
415 Notes: FE results^a represents the failure mode of SAA-BRBs, in which “S” represents “stable”; “GB” represents “global buckling”.



(a) Group 1 ($A_c=4356 \text{ mm}^2$)

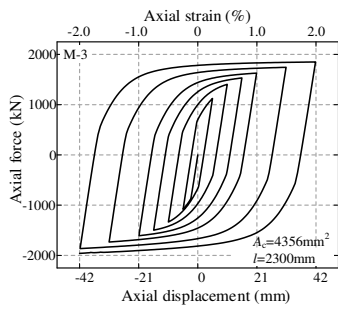


(b) Group 2 ($A_c=4796 \text{ mm}^2$)

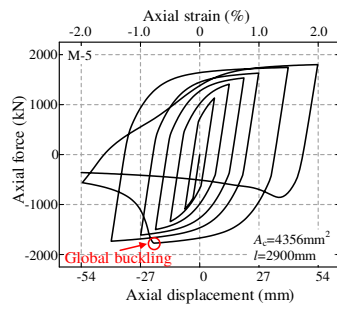


(c) Group 3 ($A_c=6556 \text{ mm}^2$)

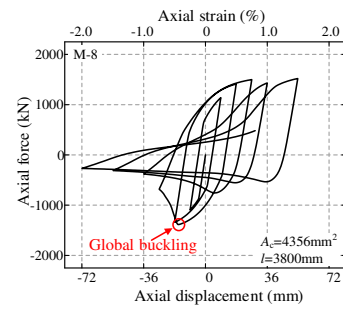
Fig. 17 Verification of restraining ratio requirements



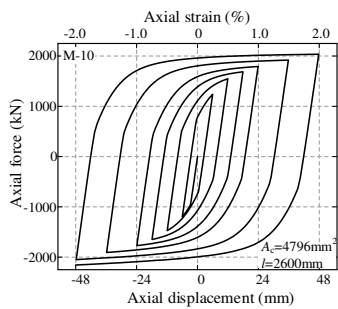
(a) M-3 ($\zeta=2.88$, $[\zeta]=2.06$)



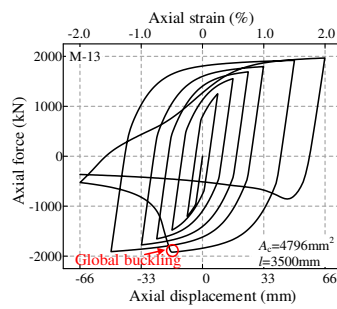
(b) M-5 ($\zeta=1.82$, $[\zeta]=2.15$)



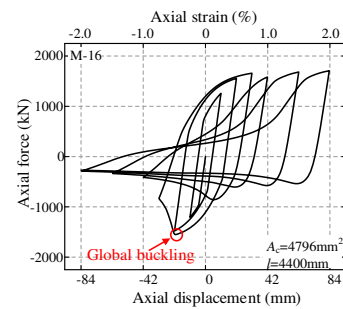
(c) M-8 ($\zeta=1.07$, $[\zeta]=2.30$)



(d) M-10 ($\zeta=2.44$, $[\zeta]=2.01$)



(e) M-13 ($\zeta=1.69$, $[\zeta]=2.07$)



(f) M-16 ($\zeta=1.08$, $[\zeta]=2.18$)

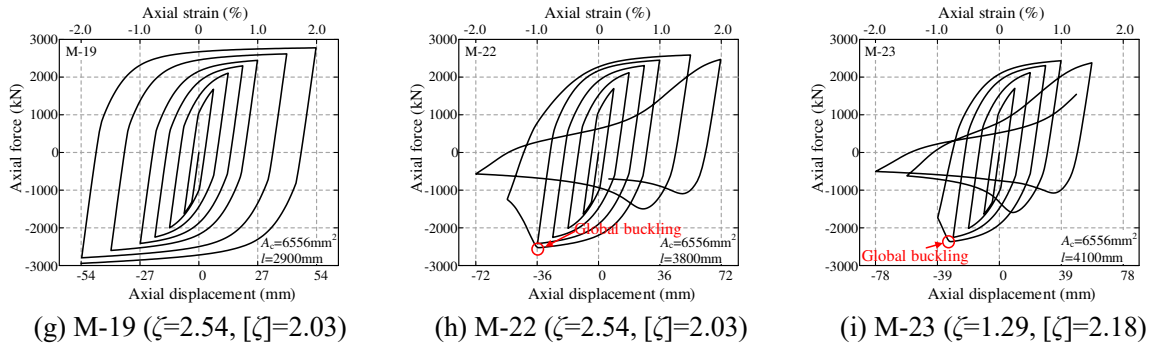


Fig. 18 Hysteretic curves of FE models

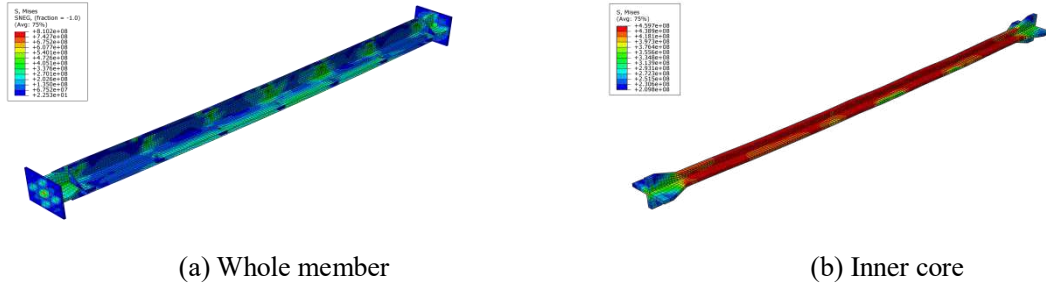


Fig. 19 Stress distribution of the SAA-BRB (model M-3)

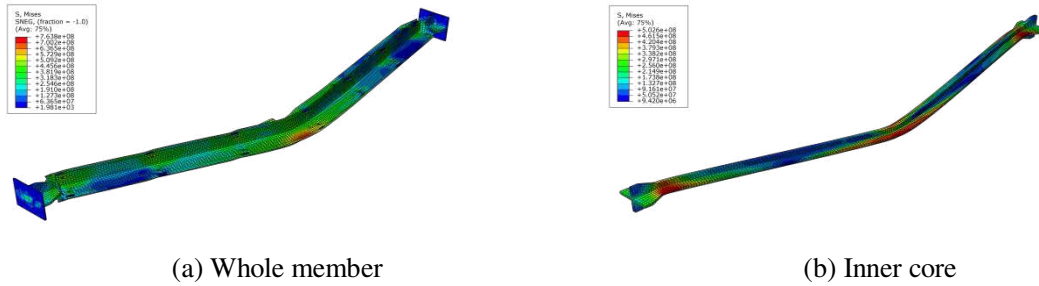


Fig. 20 Stress distribution of the SAA-BRB (model M-13)

416 6 Conclusions

417 In this study, the hysteretic responses of steel-angles-assembled buckling-restrained brace
 418 (SAA-BRB) were investigated experimentally and numerically. A design formula of restraining
 419 ratio requirements with high accuracy for predicting the global buckling of SAA-BRB was
 420 proposed and verified by parametric FE hysteretic analysis. The following conclusions can be
 421 drawn:

422 (1) Through the experiments conducted on three specimens, the hysteretic curves and
 423 skeleton curves were obtained. It is found from the experimental results that all specimens
 424 maintained stable without global buckling, indicating that a proper-designed SAA-BRB can
 425 exhibit satisfactory hysteretic performance under cyclic loads. Based on the analysis of results
 426 from the experiments, it is found that the maximum equivalent viscous damping ratios of all

427 specimens are greater than 0.5 and the compression strength adjustment factors are lower than
428 1.50 as specified in AISC. This shows that the SAA-BRB has favorable load-carrying
429 performance and energy-dissipating capacity. In addition, the plane-section assumption is
430 violated for SAA-BRB by analyzing the longitudinal strain distribution of the restraining system.

431 (2) A refined FE model considering geometric nonlinearity and material nonlinearity was
432 established. It is demonstrated that the results from FE analysis were consistent with those
433 obtained from experiments, indicating the validity of the established model in predicting the
434 hysteretic responses of SAA-BRB.

435 (3) Based on the yielding criteria of outmost fiber for the restraining system section, the
436 theoretical calculation formula of restraining ratio requirements $[\zeta]$ is derived. A parametric
437 analysis involving 24 FE models was performed to investigate the accuracy of the proposed
438 formula. It is verified that the proposed formula of restraining ratio requirement $[\zeta]$ is suitable
439 for global buckling design of SAA-BRB in engineering practice.

440 **References**

- 441 AISC (2016) Seismic provisions for structural steel buildings. AISC, Chicago
- 442 Ariyaratana C, Fahnestock LA (2011) Evaluation of buckling-restrained braced frame seismic performance
443 considering reserve strength. *Eng Struct* 33(1):77-89. <https://doi.org/10.1016/j.engstruct.2010.09.020>
- 444 Black CJ, Makris N, Aiken ID (2004) Component testing, seismic evaluation and characterization of Buckling-
445 Restrained braces. *Journal of structural engineering* (New York, N.Y.) 130(6):880-894.
446 [https://doi.org/10.1061/\(ASCE\)0733-9445\(2004\)130:6\(880\)](https://doi.org/10.1061/(ASCE)0733-9445(2004)130:6(880))
- 447 Chou C, Chen S (2010) Subassemblage tests and finite element analyses of sandwiched buckling-restrained braces.
448 *Eng Struct* 32(8):2108-2121. <https://doi.org/10.1016/j.engstruct.2010.03.014>
- 449 Chou C, Hsiao C, Chen Z, Chung P, Pham D (2019) Seismic loading tests of full-scale two-story steel building
450 frames with self-centering braces and buckling-restrained braces. *Thin Wall Struct* 140:168-181.
451 <https://doi.org/10.1016/j.tws.2019.03.024>
- 452 Dehghani M, Tremblay R (2018) Design and full-scale experimental evaluation of a seismically enduring steel
453 buckling-restrained brace system. *Earthq Eng Struct D* 47(1):105-129. <https://doi.org/10.1002/eqe.2941>
- 454 Ding YK (2014) Cyclic tests for unbonded steel plate brace encased in reinforced concrete panel or light-weight
455 assembled steel panel. *J Constr Steel Res* 94:91-102. <https://doi.org/10.1016/j.jcsr.2013.11.009>
- 456 Eryasar ME, Topkaya C (2010) An experimental study on steel-encased buckling-restrained brace hysteretic
457 dampers. *Earthq Eng Struct D* 39(5):561-581. <https://doi.org/10.1002/eqe.959>
- 458 Fujimoto M (1988) A study on the unbonded brace encasted in bucking-restrained concrete and steel tube. *Journal*
459 *of Str. Engineering, AIJ* 34
- 460 Fujimoto M, Wada A, Saeki E, Takeuchi T, Watanabe A (1990) Development of unbonded brace. *Quarterly*
461 *Column* 115(1):91-96
- 462 GB (2010) Code for seismic design of buildings. China Plan Publishing Company, Beijing
- 463 GB (2017) Code for design of steel structures. China Plan Publishing Company, Beijing
- 464 Guo Y, Fu P, Zhou P, Tong J (2016) Elastic buckling and load resistance of a single cross-arm pre-tensioned cable
465 stayed buckling-restrained brace. *Eng Struct* 126:516-530
- 466 Guo Y, Zhang B, Zhu B, Zhou P, Zhang Y, Tong J (2017a) Theoretical and experimental studies of battened
467 buckling-restrained braces. *Eng Struct* 136:312-328. <https://doi.org/10.1016/j.engstruct.2017.01.034>
- 468 Guo Y, Tong J, Zhang B, Zhu B, Pi Y (2017b) Theoretical and experimental investigation of core-separated
469 buckling-restrained braces. *J Constr Steel Res* 135:137-149. <https://doi.org/10.1016/j.jcsr.2017.04.019>
- 470 Guo Y, Tong J, Wang X, Zhang B (2017c) Subassemblage tests and numerical analyses of buckling-restrained
471 braces under pre-compression. *Eng Struct* 138:473-489. <https://doi.org/10.1016/j.engstruct.2017.02.046>
- 472 Guo Y, Tong J, Wang X, Zhou P (2018) Subassemblage tests and design of steel channels assembled buckling-
473 restrained braces. *B Earthq Eng* 16(9):4191-4224. <https://doi.org/10.1007/s10518-018-0337-5>
- 474 Guo Y, Zhang B, Jiang Z, Chen H (2015) Critical load and application of core-separated buckling-restrained
475 braces. *J Constr Steel Res* 106:1-10. <https://doi.org/10.1016/j.jcsr.2014.11.011>
- 476 Guo Y, Zhou P, Andrew Bradford M, Pi Y, Tong J, Fu P (2017) Theoretical and numerical studies of elastic
477 buckling and load resistance of double cross-arm pre-tensioned cable stayed buckling-restrained braces. *Eng*
478 *Struct* 153:674-699. <https://doi.org/10.1016/j.engstruct.2017.10.064>
- 479 Hosseinzadeh S, Mohebi B (2016) Seismic evaluation of all-steel buckling restrained braces using finite element
480 analysis. *J Constr Steel Res* 119:76-84. <https://doi.org/10.1016/j.jcsr.2015.12.014>
- 481 JGJ (2015) Specification for seismic test of building. China Plan Publishing Company, Beijing

482 Jia L, Ge H, Maruyama R, Shinohara K (2017) Development of a novel high-performance all-steel fish-bone
483 shaped buckling-restrained brace. *Eng Struct* 138:105-119. <https://doi.org/10.1016/j.engstruct.2017.02.006>

484 Jiang ZQ, Guo YL, Zhang AL, Dou C, Zhang CX (2017) Experimental study of the pinned double rectangular
485 tube assembled buckling-restrained brace. *J Zhejiang Univ-Sc a* 18(1):20-32.
486 <https://doi.org/10.1631/jzus.A1600483>

487 Ju YK, Kim M, Kim J, Kim S (2009) Component tests of buckling-restrained braces with unconstrained length.
488 *Eng Struct* 31(2):507-516. <https://doi.org/10.1016/j.engstruct.2008.09.014>

489 Judd JP, Marinovic I, Eatherton MR, Hyder C, Phillips AR, Tola AT, Charney FA (2016) Cyclic tests of all-steel
490 web-restrained buckling-restrained brace subassemblages. *J Constr Steel Res* 125:164-172.
491 <https://doi.org/10.1016/j.jcsr.2016.06.007>

492 Kiggins S, Uang C (2006) Reducing residual drift of buckling-restrained braced frames as a dual system. *Eng*
493 *Struct* 28(11):1525-1532. <https://doi.org/10.1016/j.engstruct.2005.10.023>

494 Metelli G, Bregoli G, Genna F (2016) Experimental study on the lateral thrust generated by core buckling in
495 bolted-BRBs. *J Constr Steel Res* 122:409-420. <https://doi.org/10.1016/j.jcsr.2016.04.004>

496 Mirtaheri SM, Nazeryan M, Bahrani MK, Nooralizadeh A, Montazerian L, Naserifard M (2017) Local and global
497 buckling condition of all-steel buckling restrained braces. *Steel Compos Struct* 23(2):217-228.
498 <https://doi.org/https://doi.org/10.12989/scs.2017.23.2.217>

499 Mochizuki S, Murata Y, Andou N, Takahashi S (1979) Experimental study on buckling of unbonded braces under
500 axial forces: Parts 1 and 2. In: Summaries of technical papers of annual meeting. Architectural Institute of
501 Japan, pp 1623-1626

502 Nagao T, Sera S, Nakamura S, Ouchi H, Otani K, Fukutajima K (1992) A study on the RC encased H-section
503 steel brace (Part 1: General description, Part 2: Results and discussion). In: Summaries of Technical Papers
504 of Annual Meeting of the Architectural Institute of Japan, Structural Engineering Section II, Tokyo, Japan:
505 AIJ, pp 1773-1776

506 Palazzo G, López-Almansa F, Cahís X, Crisafulli F (2009) A low-tech dissipative buckling restrained brace.
507 Design, analysis, production and testing. *Eng Struct* 31(9):2152-2161.
508 <https://doi.org/10.1016/j.engstruct.2009.03.015>

509 Shi Q, Wang F, Wang P, Chen K (2018) Experimental and numerical study of the seismic performance of an all-
510 steel assembled Q195 low-yield buckling-restrained brace. *Eng Struct* 176:481-499.
511 <https://doi.org/10.1016/j.engstruct.2018.09.039>

512 Takeuchi T, Hajjar JF, Matsui R, Nishimoto K, Aiken ID (2010) Local buckling restraint condition for core plates
513 in buckling restrained braces. *J Constr Steel Res* 66(2):139-149

514 Timoshenko SP, Gere JM, Prager W (1962) Theory of elastic stability. *Journal of Applied Mechanics* 29(1):220

515 Tong J, Guo Y (2017) Global buckling prevention of end collared buckling-restrained braces: Theoretical,
516 numerical analyses and design recommendations. *Eng Struct* 152:289-306.
517 <https://doi.org/10.1016/j.engstruct.2017.09.014>

518 Tong J, Guo Y (2018) Numerical investigations on elastic buckling and hysteretic behavior of steel angles
519 assembled buckling-restrained braces. *J Constr Steel Res* 144:21-39.
520 <https://doi.org/10.1016/j.jcsr.2018.01.015>

521 Tong J, Guo Y, Pan W, Shen M, Zhou P (2020) Global buckling prevention of reduced-core-length buckling-
522 restrained braces: Theoretical and numerical investigations. *B Earthq Eng* 18(4):1777-1804.
523 <https://doi.org/10.1007/s10518-019-00768-0>

- 524 Tremblay R, Bolduc P, Neville R, Devall R (2006) Seismic testing and performance of buckling-restrained bracing
525 systems. *Can J Civil Eng* 33(2):183-198. <https://doi.org/10.1139/L05-103>
- 526 Yoshino T, Karino Y (1971) Experimental study on shear wall with braces: Part 2. In: *Summaries of technical*
527 *papers of annual meeting*. Architectural Institute of Japan, pp 403-404
- 528 Zhao J, Lin F, Wang Z (2017) Seismic design of buckling-restrained brace welded end connection considering
529 frame action effects: Theoretical, numerical and practical approaches. *Eng Struct* 132:761-777.
530 <https://doi.org/10.1016/j.engstruct.2016.11.069>
- 531 Zhao J, Wu B, Ou J (2013) Global stability design method of buckling-restrained braces considering end bending
532 moment transfer: Discussion on pinned connections with collars. *Eng Struct* 49:947-962.
533 <https://doi.org/10.1016/j.engstruct.2012.12.042>

534 **Declaration**

535 The authors declare that they have no known competing financial interests or personal
536 relationships that could have appeared to influence the work reported in this paper.

537 **Acknowledgments**

538 This study has been supported by research grants from the National Natural Science
539 Foundation of China (52108180) and the Zhejiang Provincial Natural Science Foundation of
540 China (LQ21E080018).